

Coupling Borophene to Graphene in Air-Stable Heterostructures

Matteo Jugovac,* Iulia Cojocariu, Carlo Alberto Brondin, Alessandro Crotti, Marin Petrović, Stefano Bonetti, Andrea Locatelli, and Tevfik Onur Mentesh*

Artificial 2D van der Waals heterostructures with controllable vertical stacking and rotational orientation exhibit multifaceted electronic properties that are appealing for applications in fields ranging from optoelectronics to energy storage. Along with transition metal dichalcogenides and graphene, borophene has recently emerged as a promising building block for 2D devices due to its conductive nature as well as its exceptional mechanical and electronic properties. Here, it is demonstrated that the combination of the dissolution-segregation process and chemical vapor deposition allows for the synthesis of graphene/borophene heterostructures of the highest crystalline and chemical quality, in which graphene sits on top of the borophene layer with metallic character. The formation of laterally distinct micron-sized areas allows a comparative study of borophene, graphene, and the graphene–borophene heterostack in terms of their electronic properties and stability in a reactive environment. Whereas pristine borophene is particularly prone to oxidation, the graphene–borophene heterostack is chemically inert and enables the conservation of borophene’s character even after exposure to air. This study opens up new perspectives for the scalable synthesis of graphene–borophene heterostacks with enhanced ability to preserve the metallic character and electronic properties of borophene.

where different 2D materials, e.g., conductors (e.g., graphene), semiconductors with varying bandgaps (e.g., black phosphorus, MoS₂, and WSe₂) and insulators (e.g., boron nitride (BN)) were used to demonstrate prototype devices such as transistors, detectors, solar cells, batteries.^[2–5] In the still-growing field of 2D materials, graphene, with its superior physical, optical, and electronic properties, apart from its robustness and inertness, is often a fundamental building block in the fabrication of heterostructures for efficient and long-lasting devices.^[6]

Borophene, a 2D polymorphic form of boron,^[7] is closely related to graphene, as it is a mono-elemental 2D material characterized by a hexagon-like structure capable of hosting Dirac quasiparticles.^[8–10] However, contrary to graphene, which is inert, borophene is highly reactive. While this reactivity can be an advantage when considering borophene as a catalyst, its tendency toward oxidation can strongly affect its pristine properties.^[11–13] To

date, the issue of borophene chemical instability^[14] has been tackled by hydrogenation of the layer^[15] or by capping it with a hexagonal boron nitride layer (hBN).^[16] The insulating nature of hBN dictates that the conducting properties of the borophene–hBN vertical heterostructures are driven by the metallicity of borophene itself, especially since no electronic interaction was

1. Introduction

2D heterostructures composed of stacked Van der Waals materials exhibit controllable electronic, magnetic, and optical properties.^[1] In this respect, numerous studies were devoted to the fabrication and characterization of vertical heterostructures,


M. Jugovac, I. Cojocariu, C. A. Brondin, A. Locatelli, T. O. Mentesh
Elettra – Sincrotrone Trieste S.C.p.A.
S.S. 14 km 163.5, Trieste 34149, Italy
E-mail: matteo.jugovac@elettra.eu; tevfik.mentesh@elettra.eu

I. Cojocariu
Dipartimento di Fisica
Università degli studi di Trieste
Via A. Valerio 2, Trieste 34127, Italy

C. A. Brondin, A. Crotti, S. Bonetti
Department of Molecular Sciences and Nanosystems
Ca’ Foscari University of Venice
via Torino 155, Venice 30172, Italy

M. Petrović
Center of Excellence for Advanced Materials and Sensing Devices
Institute of Physics
Bijenička 46, Zagreb 10000, Croatia

S. Bonetti
Department of Physics
Stockholm University
Stockholm 10691, Sweden

 The ORCID identification number(s) for the author(s) of this article can be found under <https://doi.org/10.1002/aelm.202300136>

© 2023 The Authors. Advanced Electronic Materials published by Wiley-VCH GmbH. This is an open access article under the terms of the Creative Commons Attribution License, which permits use, distribution and reproduction in any medium, provided the original work is properly cited.

DOI: 10.1002/aelm.202300136

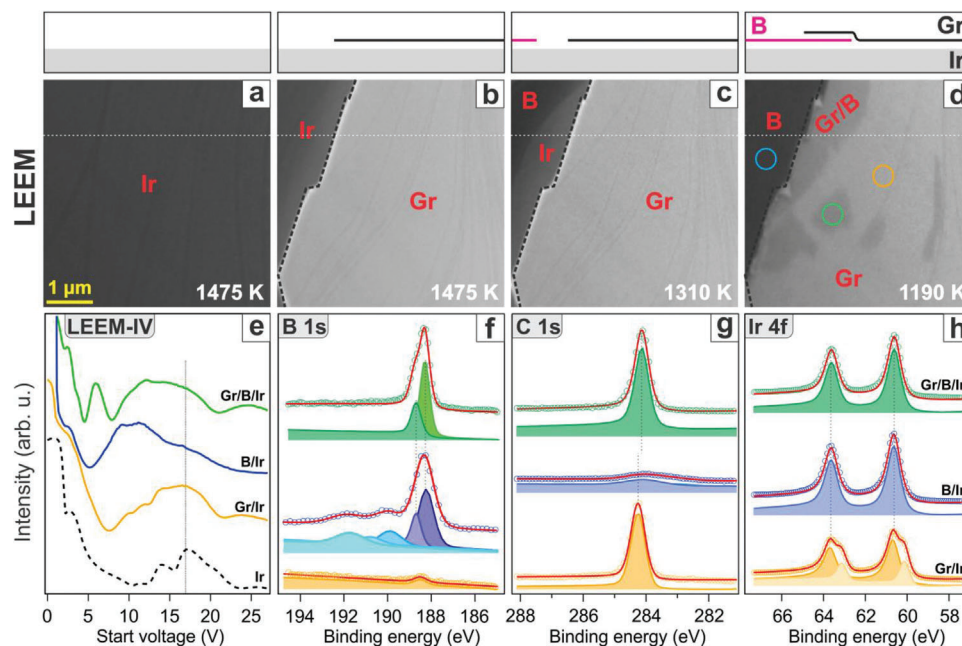


Figure 1. Growth and spectroscopic characterization of the graphene/borophene heterostructure. a–d) LEEM image sequence ($V_{st} = 17$ V) acquired during the synthesis, in which a clean Ir(111) crystal (a), enriched with B in the bulk, is exposed to ethylene until a graphene (Gr) layer is formed (b). During cooling, boron islands appear first in the graphene-uncovered regions (c), and subsequently underneath graphene (b) by lowering the temperature further (d). Schematic cross-sectional view of each growth step along the horizontal dotted line is given above LEEM images. e) LEEM-IV spectra acquired on four distinct surface areas (vertical line indicates the energy selected for imaging in a–d). Core-level XPS spectra of Gr/Ir, B/Ir and Gr/B/Ir are shown on: f) B 1s, g) C 1s and h) Ir 4f.

observed between the two. Instead, by interfacing borophene with a conductive, albeit inert, material such as graphene, an increased electron density, and thus a boost in the electrochemical performances is predicted.^[17] Recently, this density functional theory (DFT) prediction has been experimentally realized in a borophene–graphene-based anode for Li-ion batteries, which exhibits increased specific capacity, still far from the DFT predicted values, due to the quality of the interface.^[18]

Here, we report on the in situ synthesis and spectroscopic characterization of a graphene–borophene vertical stack. All the growth steps toward the synthesis of the graphene–borophene heterostructure are monitored by means of in operando low-energy electron microscopy (LEEM). The growth procedure reported here leads to an enhanced crystallographic and chemical quality in the vertical heterostructure, as revealed by micro-spot low-energy electron diffraction (μ LEED) and x-ray photoemission microscopy (XPEEM). The micro-spot angle-resolved photoemission (μ ARPES) spectrum of the heterostack is dominated by graphene Dirac cones in addition to a state with parabolic dispersion deriving from borophene. The presence of borophene bands in the proximity of the Fermi level leads to an enhancement in the heterostructure’s density of states (DOS) compared to monolayer graphene. The increased DOS correlates with the boost in the electrochemical performances of graphene–borophene with respect to graphene alone, as previously predicted by DFT.^[17] Moreover, by exposing the heterostructure to ambient conditions, we demonstrate its enhanced chemical stability. Indeed, the borophene layer in the graphene–borophene heterostructure retains its metallic character and proves to be less prone to oxidation, even in a highly reactive environment.

2. Results and Discussion

In our experiments, boron is provided by the dissociative adsorption of borazine ($B_3N_3H_6$) on the clean Ir(111) single crystal surface at 1375 K. An increase in the sample temperature to 1475 K leads to dissolution and accumulation of boron in the Ir bulk, as well as desorption of H and N from the surface (see Figure 1a). While still at high temperature, the boron-enriched iridium crystal is then exposed to ethylene at a partial pressure of 5×10^{-7} mbar, which induces the nucleation and growth of single-crystal graphene flakes several microns in size with monolayer thickness. (Figure 1b).^[19] Ultra-high Vacuum (UHV) conditions are restored when graphene islands and uncovered substrate regions coexist in equal amounts, as shown in the LEEM image in Figure 1b. Subsequently, the sample temperature is lowered below the boron segregation temperature (i.e., 1320 K), enough to trigger boron segregation and subsequent borophene formation on Ir(111)^[20,21] in the graphene-free regions, which is manifested by the propagation of the growth front appearing slightly brighter than the substrate in LEEM (Figure 1c). When the sample temperature is further reduced to below 1200 K, a new phase is observed within the graphene-covered islands, appearing with lesser intensity in LEEM at the chosen electron energy (Figure 1d). The sample is then cooled down to room temperature, which does not produce any changes in the surface morphology as imaged by LEEM.

The resulting surface shows distinctly different regions, each exhibiting a well-defined low energy electron reflectivity (LEEM-IV) curve, as seen in Figure 1e. The boron-covered areas outside graphene show the same LEEM-IV previously obtained for

monolayer borophene on Ir(111).^[22] On most parts of the graphene-covered region (bright regions in Figure 1d), the characteristic LEEM-IV curve for single-layer graphene on Ir(111) can be observed.^[23] Instead, in the darker areas, a strikingly different reflectivity curve is measured, exhibiting two minima at low electron energies. These minima are reminiscent of quantum well state oscillations in LEEM-IV curves of multilayer graphene films^[24–27] or graphene/hBN heterostacks.^[28] Therefore, the reflectivity curve of region “Gr/B” in Figure 1d is consistent with a stack of well-defined 2D layers in close contact with each other. We note that the lateral dimension of these islands underneath graphene can be tuned by varying the concentration of dissolved B in the Ir crystal, or by surface deposition and subsequent intercalation of additional boron while keeping the sample at 670 K (see Figure S1, Supporting Information).

The different chemistry of the three distinct surface regions observed in LEEM can be better understood by laterally-resolved x-ray photoemission spectroscopy (XPS) on the relevant core levels (B 1s, C 1s, and Ir 4f). Boron-covered Ir(111) surface outside the graphene islands appears to contain more than one chemically non-equivalent species. The main contribution to the B 1s core level is well-described by a sum of two Voigt-like functions at 188.35 and 188.75 eV binding energy, as seen in Figure 1f (middle spectrum). These peaks might be associated with a different chemical environment of boron atoms in borophene, i.e., different coordination numbers. The other B 1s peaks at higher binding energies, 189.93, 190.97 and 191.90 eV are identified with the presence of BC_2O , BCO_2 , and B_2O_3 species, respectively.^[29–31] This indicates that the borophene layer (B/Ir) has been partially contaminated due to exposure to residual gases in the UHV chamber over the timescale of 12 h needed to complete these post-synthesis XPS measurements.

Within the parts of the graphene islands with the typical LEEM-IV curve of single layer Gr/Ir(111), a small B 1s peak can be seen at 188.48 eV (Figure 1f, bottom spectrum), which could be attributed to the formation of boron clusters with lateral size below the spatial resolution limit of the microscope. Instead, in the regions denoted as Gr/B/Ir, a sharp and prominent B 1s peak is observed. The entire B 1s spectrum can be fitted using two components at 188.35 and 188.75 eV binding energies, in close agreement with the spectrum recorded at borophene on Ir(111). Although at the same binding energy, these peaks have a 43% smaller FWHM with respect to the main peak of borophene (at lower binding energies) found in the regions not covered by graphene. This further hints at the presence of a borophene layer at the graphene-Ir interface with high structural quality and chemical purity.

The graphene layer spectroscopically shows only subtle differences with and without the borophene layer underneath, as can be seen in Figure 1g. C 1s peak of Gr/Ir regions is found at 284.22 eV, in agreement with pristine graphene on Ir(111).^[32] In comparison, C 1s from the Gr/B/Ir regions has a 0.13 eV shift toward lower binding energies. The presence of such a shift can be justified with electron final-state screening effects, originating from the different graphene support, B or Ir.^[33] Integrated C 1s intensity in the two regions is the same, confirming no compositional differences between graphene in Gr/Ir and Gr/B/Ir. On the other hand, the Ir 4f surface core level^[34] is visible when Ir(111) is covered with graphene (Figure 1h, bottom spectrum), while it

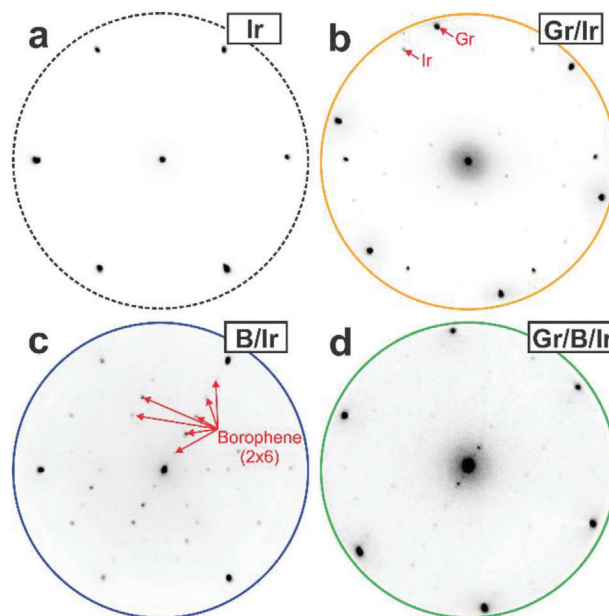


Figure 2. Structural characterization of the four distinct areas shown in Figure 1. LEED patterns are acquired at 40 eV electron energy for a) clean Ir(111), b) Gr/Ir, c) B/Ir (c) and d) Gr/B/Ir heterostack.

disappears in the presence of borophene at the graphene-Ir interface (Figure 1h, top spectrum).

The crystalline structure of the different surface phases visible in Figure 1 is probed using μ -LEED. The (1×1) LEED pattern from the clean Ir(111) surface shown in Figure 2a is attenuated when the surface is covered with graphene (Figure 2b). As noted previously, the graphene growth protocol we employed led to the formation of islands with different rotational configurations. For the particular graphene flake shown in Figure 2b, the azimuthal rotation between the high symmetry directions of graphene and Ir(111) is found to be 17° , identified with a $\text{Gr}(\sqrt{79} \times \sqrt{79})/\text{Ir}(8 \times 8)$ structure.^[35] The (2×6) -reconstructed LEED pattern from the B/Ir region (Figure 2c) is consistent with the single domain χ_6 structure reported for borophene on Ir(111).^[20] A similar (2×6) reconstruction can be discerned in the μ -LEED pattern from the Gr/B/Ir region, as seen in Figure 2d, along with the graphene and Ir(111) diffraction spots (the LEED pattern in logarithmic color scale is shown in Figure S2a, Supporting Information). Thus, the LEED data clearly support the conclusion from XPS and LEEM-IV measurements that commensurate borophene islands form at the Gr/Ir interface.

It should be noted that borophene always grows in registry with the Ir(111) substrate, independently of whether there is a graphene layer on top. Therefore, the angle between graphene and borophene in the heterostack can be varied according to the Gr-Ir rotational alignment (shown in more detail in Figure S2b–e, Supporting Information). In other words, a series of graphene-borophene interlayer stacking angles reflect the angles observed at the Gr-Ir interface.^[19,35] Notably, graphene islands epitaxially aligned to Ir(111) ($R0^\circ$ graphene) constitute an exception. Differently from all other graphene rotations, we do not find the segregation of borophene underneath the $R0^\circ$ graphene. Such behavior is reminiscent of the growth of bilayer graphene on Ir(111),

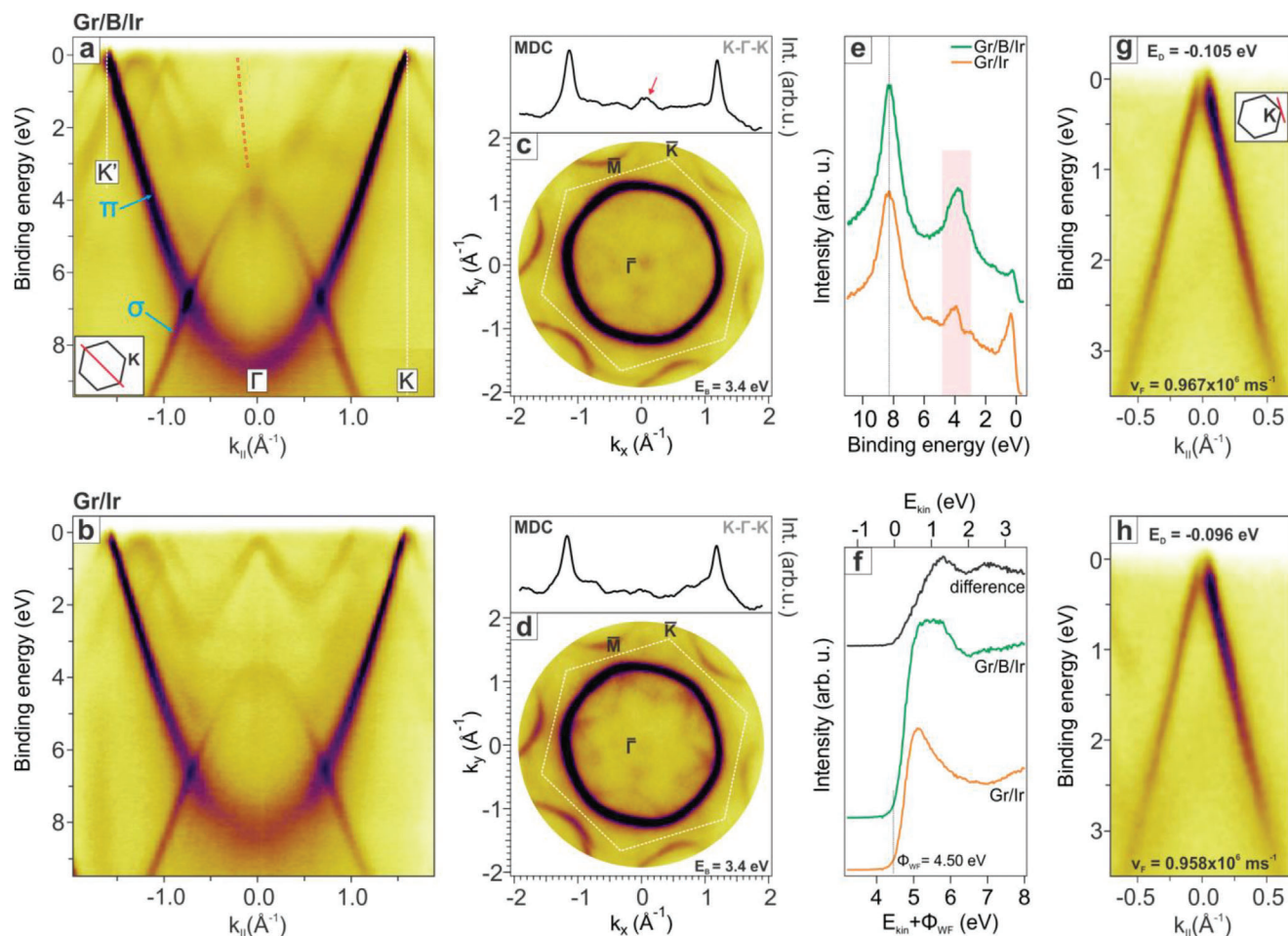


Figure 3. Electronic structure comparison of Gr/Ir and Gr/B/Ir. Energy versus momentum distribution acquired along the $K\Gamma K$ direction of the SBZ of Gr/B/Ir (a) and Gr/Ir (b). Constant binding energy momentum map at 3.4 eV binding energy of Gr/B/Ir (c) and Gr/Ir (d) are shown. Respective intensity profiles along $K\Gamma K$ can be seen on top of each map. e) Normal emission photoemission spectra and f) secondary photoelectron emission spectra of the two interfaces are displayed along with the difference spectrum for the latter. Energy versus momentum distribution acquired at the K point of Gr/B/Ir (g) and Gr/Ir (h) along the profile shown in the inset.

where the second layer of graphene easily forms below rotated graphene while it is not favored under $R0^\circ$ graphene.^[26] This in turn can be related to stronger Gr-Ir interaction in the $R0^\circ$ phase as compared to misaligned phases.^[36]

The electronic structure of Gr/Ir and Gr/B/Ir were probed using μ -ARPES. The corresponding energy versus momentum maps, acquired along the $K\Gamma K$ direction of the graphene surface Brillouin zone (SBZ) (as indicated in the inset of Figure 3a), are plotted in Figure 3a,b, respectively. Graphene π and σ bands, as indicated in Figure 3a, constitute the most prominent features in both spectra. The W-shaped band, identified as the Ir surface state, is clearly visible for Gr/Ir (especially at Γ), while it is partially suppressed in the case of Gr/B/Ir due to the strong interaction between boron and Ir(111). Note that this is closely connected to the reduction in the Ir 4f surface core level peak in Gr/B/Ir, as it was shown in Figure 1h.

In the energy versus momentum map of Gr/B/Ir, a parabolic band centered at Γ and characterized by a vertex between 3.5 and 4.5 eV binding energy is present (the second derivative plot is depicted in Figure S3, Supporting Information). This state is asso-

ciated with borophene, as previously predicted by Penev et al.,^[37] and it is most visible using vertically-polarized x-rays due to its p_z character. Its presence is better appreciated in the 2D momentum maps acquired at a binding energy of 3.4 eV and plotted in Figure 3c. The associated momentum distribution curve (MDC) shows an enhanced contribution at the Γ point of the SBZ, as compared to the Gr/Ir case (Figure 3d). This enhancement is clearly seen in the photoemission intensity at the Γ point as a peak centered at 4 eV binding energy (Figure 3e). Interestingly, the position of the graphene π band bottom in Gr/B/Ir does not present any significant shift as compared to Gr/Ir. This is also true for the graphene Dirac point, which is plotted in Figure 3g,h. By fitting the linearly-dispersing bands, the Dirac point is found at nearly identical energies in the two cases. Similarly, no significant difference is found in the Fermi velocity of the π bands. This behavior is in line with previously published results on vertical heterostacks of graphene with other 2D materials, where the graphene π band was only slightly affected^[38,39] or not perturbed at all.^[40,41] However, it should be noted that, since no significant difference is observed in the position of graphene Dirac cones,

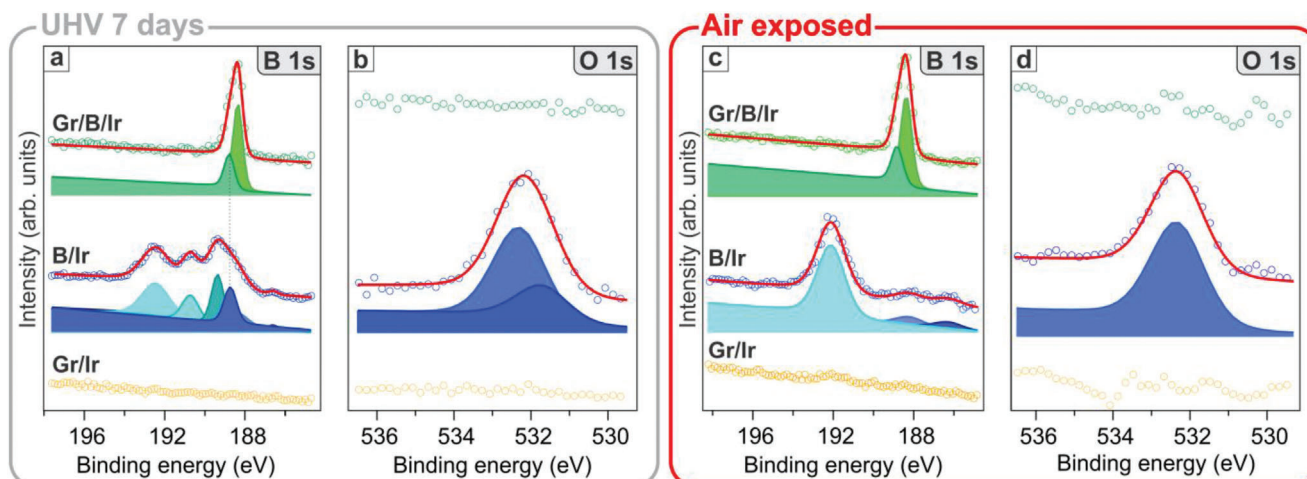


Figure 4. Stability of the interface in vacuum and upon air exposure. Comparison of B 1s and O 1s spectra, measured on three distinct regions, after 7 days in the UHV chamber (left panel – a and b) and upon 90 min air exposure (right panel – c and d).

the presence of the parabolic state in the proximity of the Fermi level leads to an increased DOS in the graphene–borophene heterostructure. Such enhanced DOS is likely responsible for an enhancement in the electrochemical activity of the graphene–borophene heterostructure when employed as an anode in the Li-ion spectra.^[18]

Consistently with the observations on the valence band spectra, the work functions of Gr/Ir and Gr/B/Ir are found to be nearly the same via photoelectron threshold measurements (Figure 3f). Beyond the determination of work function, the secondary photoemission spectrum obtained by the difference between the two spectra provides information about the unoccupied band structure of the borophene layer.^[42] Such a difference spectrum in Figure 3g shows two prominent peaks at 1.1 and 2.5 eV kinetic energy. This compares well with the previously published DFT calculations of the total density of states above the Fermi level of monolayer borophene in a χ_6 phase on Ir(111),^[43] where the peaks are observed at around -1.5 and -3 eV.

Finally, the chemical stability of the different surface phases was tested by keeping the sample in ultra-high vacuum conditions for an extended period of time (7 days after growth, in the following called UHV7) and by exposing the sample to air (in the following called AE). The dramatic changes in the B 1s spectrum of B/Ir for UHV7 (Figure 4a), as compared to the as-synthesized one (Figure 1g), demonstrate that the borophene layer is very reactive and is easily contaminated even under UHV conditions. In particular, the peaks related to BC_2O , BCO_2 , and B_2O_3 are significantly higher in intensity as compared to the initial characterization shown in Figure 1f, while the peaks assigned to pristine borophene on Ir are remarkably lower in intensity. Moreover, the appearance of a small contribution at lower binding energies related to the formation of carbon-decorated boron, centered at 187.15 eV, can be observed.^[44] Instead, the B 1s spectrum of the Gr/B/Ir heterostack does not present any changes with respect to the as-synthesized sample. The analysis of the O 1s core level emission confirms the above observations, where oxygen is only observed in the borophene/Ir regions. The spectrum is deconvoluted into two components, assigned to the emission from boron

oxide (532.30 eV)^[30] and to the emission from BC_xO_y species (531.70 eV).^[31]

By exposing the sample to air, the B 1s spectra (Figure 4c) in the B/Ir regions are characterized by an almost full transition to boron oxide, with only minor peak contributions at lower binding energies. This behavior is confirmed in the O 1s spectrum, which is characterized by a single peak assigned to boron oxide (532.30 eV). Remarkably, contrary to what has been observed for pristine monolayer borophene synthesized on top of Ag^[11,12] and Cu,^[13] which easily oxidizes, the graphene-capped borophene (Gr/B/Ir) preserves its pristine XPS lineshape and intensity even under ambient conditions ($t = 90$ min). No sign of degradation or oxidation is noted, as confirmed by the O 1s spectrum. Therefore, we conclude that the graphene layer in the heterostack fully protects the borophene layer from oxidation in highly reactive environments.

3. Conclusion

A novel synthesis procedure, based on CVD and annealing in UHV, was employed for synthesizing graphene–borophene vertical heterostructures, presenting an atomically sharp interface with superior chemical quality. In particular, on top of a boron-enriched Ir crystal, monolayer graphene is synthesized at high temperatures. The controlled lowering of sample temperature leads to boron segregation and the formation of borophene islands below graphene. The resulting twisted graphene–borophene heterostacks show enhanced stability and resilience toward oxidation, with the boron monolayer that preserves its metallic character even upon air exposure. The electronic structure of the heterostructure is characterized by sharp graphene Dirac cones along with a parabolic band with π -character. The presence of such a metallic-like state of borophene, crossing the Fermi level, leads to an enhancement of the electronic density of states of the heterostructure, as compared to monolayer graphene. This study explains the increased electrochemical performance of the heterostructure when employed as an anode in alkali-ion batteries, paving the way toward the

implementation of efficient and ambient-stable graphene-borophene heterostructures for energy storage devices.

4. Experimental Section

Sample preparation: The experiments were performed using an Ir(111) single crystal (MaTeck), which, prior to the 2D materials growth, was cleaned by iterative cycles of 1.5 keV argon-ion sputtering and annealing up to 1500–1600 K. Bulk carbon was removed by keeping the sample in oxygen backpressure at a temperature of 1270 K. Adsorbed surface oxygen was removed by UHV annealing at about 1700 K, until a clean and well-ordered surface was obtained, as verified by LEED and XPS.

Boron enrichment of the Ir crystal was performed by dosing borazine (Katchem) on the clean Ir(111) single crystal surface at 1375 K. By annealing the sample to 1475 K, bulk dissolution of boron accompanied by desorption of H and N from the surface, allowed accumulating boron in the Ir subsurface. Graphene was grown by exposing the sample to ethylene (SIAD, purity grade > 4.5) backpressure ($p = 5 \times 10^{-7}$ mbar) while keeping the sample at 1475 K, leading to the formation of aligned and azimuthally rotated monolayer graphene islands of several microns in size.

Instrumentation: All the experiments were performed using the Spectroscopic Photoemission and Low Energy Electron Microscope (SPELEEM III, Elmitec GmbH) operating at the “Nanospectroscopy” beamline of the Elettra synchrotron in Trieste (Italy).^[45] The sample is either illuminated with low-energy electrons (LEEM mode) or soft X-rays in the range 30–200 eV with variable polarization (XPEEM mode), providing structural and chemical sensitivity, respectively;^[46,47] the elastically backscattered or the photoemitted electrons are directly imaged on a 2D detector comprising a phosphorous screen and a CCD camera (QImaging Retiga). The electron energy is set by applying a voltage bias to the sample, commonly referred to as start voltage, V_{st} . During real space imaging, contrast apertures of 10, 30, or 100 μm are used in order to set the microscope lateral resolution by limiting its angular acceptance. The SPELEEM reaches a lateral resolution better than 10 nm in LEEM and 30 nm in XPEEM mode.^[48] In addition to real space operation, the microscope also enables diffraction imaging. The SPELEEM can perform micro Low Energy Electron Diffraction (μ -LEED) measurements using electrons and microspot Angle-Resolved Photoemission Spectroscopy (μ -ARPES), by putting an aperture in the image plane of 0.5, 1, and 5 μm in diameter. The SPELEEM microscope has been recently equipped with a new hemispherical energy analyzer (Elmitec R200), which enables a best energy resolution of 100 meV in both imaging and diffraction modes. All the photoemission spectra were acquired using linearly polarized photons with the following energies: ARPES – 40 eV, B 1s and Ir 4f – 270 eV, C 1s – 400 eV, O 1s – 650 eV. The binding energies of the core level photoemission spectra were referenced to the Fermi level. The base pressure of the experimental chamber was always below 2×10^{-10} mbar.

Supporting Information

Supporting Information is available from the Wiley Online Library or from the author.

Acknowledgements

This work was supported by the Croatian Science Foundation grant No. UIP-2020-02-1732.

Conflict of Interest

The authors declare no conflict of interest.

Data Availability Statement

The data that support the findings of this study are available from the corresponding author upon reasonable request.

Keywords

borophene, electronics, enhanced stability, graphene, heterostructures

Received: February 27, 2023

Revised: June 13, 2023

Published online: June 29, 2023

- [1] K. S. Novoselov, A. Mishchenko, A. Carvalho, A. H. Castro Neto, *Science* **2016**, 353.
- [2] S. B. Desai, S. R. Madhupathy, A. B. Sachid, J. P. Llinas, Q. Wang, G. H. Ahn, G. Pitner, M. J. Kim, J. Bokor, C. Hu, H.-S. P. Wong, A. Javey, *Science* **2016**, 354, 99.
- [3] D. Kim, S.-H. Kang, M. Slater, S. Rood, J. T. Vaughey, N. Karan, M. Balasubramanian, C. S. Johnson, *Adv. Energy Mater.* **2011**, 1, 333.
- [4] J. Li, L. Niu, Z. Zheng, F. Yan, *Adv. Mater.* **2014**, 26, 5239.
- [5] F. Schwierz, *Nat. Nanotechnol.* **2010**, 5, 487.
- [6] J. Wang, X. Mu, M. Sun, T. Mu, *Appl. Mater. Today* **2019**, 16, 1.
- [7] P. Ranjan, J. M. Lee, P. Kumar, A. Vinu, *Adv. Mater.* **2020**, 32, 2000531.
- [8] E. S. Penev, S. Bhowmick, A. Sadrzadeh, B. Yakobson, *Nano Lett.* **2012**, 12, 2441.
- [9] B. Feng, J. Zhang, S. Ito, M. Arita, C. Cheng, L. Chen, K. Wu, F. Komori, O. Sugino, K. Miyamoto, T. Okuda, S. Meng, I. Matsuda, *Adv. Mater.* **2018**, 30, 1704025.
- [10] B. Feng, O. Sugino, R.-Y. Liu, J. Zhang, R. Yukawa, M. Kawamura, T. Iimori, H. Kim, Y. Hasegawa, H. Li, L. Chen, K. Wu, H. Kumigashira, F. Komori, T.-C. Chiang, S. Meng, I. Matsuda, *Phys. Rev. Lett.* **2017**, 118, 096401.
- [11] A. J. Mannix, X.-F. Zhou, B. Kiraly, J. D. Wood, D. Alducin, B. D. Myers, X. Liu, B. L. Fisher, U. Santiago, J. R. Guest, M. J. Yacaman, A. Ponce, A. R. Oganov, M. C. Hersam, N. P. Guisinger, *Science* **2015**, 350, 1513.
- [12] B. Feng, J. Zhang, Q. Zhong, W. Li, S. Li, H. Li, P. Cheng, S. Meng, L. Chen, K. Wu, *Nat. Chem.* **2016**, 8, 563.
- [13] R. Wu, I. K. Drozdov, S. Eltinge, P. Zahl, S. Ismail-Beigi, I. Božović, A. Gozar, *Nat. Nanotechnol.* **2019**, 14, 44.
- [14] X. Liu, M. S. Rahn, Q. Ruan, B. I. Yakobson, M. C. Hersam, *Nanotechnology* **2022**, 33, 235702.
- [15] Q. Li, V. S. C. Kolluru, M. S. Rahn, E. Schwenker, S. Li, R. G. Hennig, P. Darancet, M. K. Y. Chan, M. C. Hersam, *Science* **2021**, 371, 1143.
- [16] M. G. Cuxart, K. Seufert, V. Chesnyak, W. A. Waqas, A. Robert, M.-L. Bocquet, G. S. Duesberg, H. Sachdev, W. Auwärter, *Sci. Adv.* **2021**, 7, eabk1490.
- [17] J. Yu, M. Zhou, M. Yang, Q. Yang, Z. Zhang, Y. Zhang, *ACS Appl. Energy Mater.* **2020**, 3, 11699.
- [18] J. Yu, M. Zhou, M. Yang, Y. Zhang, B. Xu, X. Li, H. Tao, *Adv. Mater. Interfaces* **2022**, 9, 2102088.
- [19] H. Hattab, A. T. N'Diaye, D. Wall, G. Jnawali, J. Coraux, C. Busse, R. van Gastel, B. Poelsema, T. Michely, F.-J. Meyer zu Heringdorf, M. Horn-von Hoegen, *Appl. Phys. Lett.* **2011**, 98, 141903.
- [20] K. M. Omambac, M. Petrović, P. Bampoulis, C. Brand, M. A. Kriegel, P. Dreher, D. Janoschka, U. Hagemann, N. Hartmann, P. Valerius, T. Michely, F. J. Meyer zu Heringdorf, M. Horn-von Hoegen, *ACS Nano* **2021**, 15, 7421.
- [21] J. Lahiri, P. Zahl, B. Wang, E. Sutter, *Nano Lett.* **2013**, 13, 276.
- [22] A. Acun, The Growth and Characterization of Silence, Germanene and Hexagonal Boron Nitride, PhD, University of Twente **2017**.
- [23] E. Loginov, S. Nie, K. Thürmer, N. C. Bartelt, K. F. McCarty, *Phys. Rev. B* **2009**, 80, 085430.
- [24] H. Hibino, H. Kageshima, F. Maeda, M. Nagase, Y. Kobayashi, H. Yamaguchi, *Phys. Rev. B* **2008**, 77, 075413.
- [25] R. M. Feenstra, M. Widom, *Ultramicroscopy* **2013**, 130, 101.

- [26] S. Nie, A. L. Walter, N. C. Bartelt, E. Starodub, A. Bostwick, E. Rotenberg, K. F. McCarty, *ACS Nano* **2011**, *5*, 2298.
- [27] A. Locatelli, G. Zamborlini, T. O. Menteş, *Carbon* **2014**, *74*, 237.
- [28] G. Lu, G. Zhang, J. Sun, X. Wang, Z. Shi, D. Jiang, H. Wang, A. Li, T. Wu, Q. Yu, X. Xie, *Carbon* **2019**, *152*, 521.
- [29] Z.-H. Sheng, H.-L. Gao, W.-J. Bao, F.-B. Wang, X.-H. Xia, *J. Mater. Chem.* **2012**, *22*, 390.
- [30] W. E. Moddeman, A. R. Burke, W. C. Bowling, D. S. Foose, *Surf. Interface Anal.* **1989**, *14*, 224.
- [31] C. W. Ong, H. Huang, B. Zheng, R. W. M. Kwok, Y. Y. Hui, W. M. Lau, *J. Appl. Phys.* **2004**, *95*, 3527.
- [32] A. B. Preobrajenski, M. L. Ng, A. S. Vinogradov, N. Mårtensson, *Phys. Rev. B* **2008**, *78*, 073401.
- [33] G. K. Wertheim, S. B. DiCenzo, S. E. Youngquist, *Phys. Rev. Lett.* **1983**, *51*, 2310.
- [34] M. Bianchi, D. Cassese, A. Cavallin, R. Comin, F. Orlando, L. Postregna, E. Golfetto, S. Lizzit, A. Baraldi, *New J. Phys.* **2009**, *11*, 063002.
- [35] L. Meng, R. Wu, L. Zhang, L. Li, S. Du, Y. Wang, H.-J. Gao, *J. Phys.: Condens. Matter* **2012**, *24*, 314214.
- [36] E. Starodub, A. Bostwick, L. Moreschini, S. Nie, F. E. Gabaly, K. F. McCarty, E. Rotenberg, *Phys. Rev. B* **2011**, *83*, 125428.
- [37] E. S. Penev, A. Kutana, B. I. Yakobson, *Nano Lett.* **2016**, *16*, 2522.
- [38] M. T. Dau, M. Gay, D. Di Felice, C. Vergnaud, A. Marty, C. Beigné, G. Renaud, O. Renault, P. Mallet, T. L.e Quang, J.-Y. Veuillen, L. Huder, V. T. Renard, C. Chapelier, G. Zamborlini, M. Jugovac, V. Feyer, Y. J. Dappe, P. Pochet, M. Jamet, *ACS Nano* **2018**, *12*, 2319.
- [39] S. Roth, F. Matsui, T. Greber, J. Osterwalder, *Nano Lett.* **2013**, *13*, 2668.
- [40] W. Jin, P.-C. Yeh, N. Zaki, D. Chenet, G. Arefe, Y. Hao, A. Sala, T. O. Mentes, J. I. Dadap, A. Locatelli, J. Hone, R. M. Osgood Jr., *Phys. Rev. B* **2015**, *92*, 201409.
- [41] C. Chen, J. Avila, S. Wang, R. Yang, G. Zhang, M. C. Asensio, *J. Phys.: Conf. Ser.* **2017**, *864*, 012005.
- [42] O. Y. Vilkov, E. E. Krasovskii, A. V. Fedorov, A. G. Rybkin, A. M. Shikin, C. Laubschat, J. Budagosky, D. V. Vyalikh, D. Y. Usachov, *Phys. Rev. B* **2019**, *99*, 195421.
- [43] N. A. Vinogradov, A. Lyalin, T. Taketsugu, A. S. Vinogradov, A. Preobrajenski, *ACS Nano* **2019**, *13*, 14511.
- [44] M. Cattelan, S. Agnoli, M. Favaro, D. Garoli, F. Romanato, M. Meneghetti, A. Barinov, P. Dudin, G. Granozzi, *Chem. Mater.* **2013**, *25*, 1490.
- [45] A. Locatelli, L. Aballe, T. O. Mentes, M. Kiskinova, E. Bauer, *Surf. Interface Anal.* **2006**, *38*, 1554.
- [46] A. Locatelli, E. Bauer, *J. Phys.: Condens. Matter* **2008**, *20*, 093002.
- [47] E. Bauer, *Surface Microscopy with Low Energy Electrons*, Springer, New York, **2014**.
- [48] T. O. Menteş, G. Zamborlini, A. Sala, A. Locatelli, *Beilstein J. Nanotechnol.* **2014**, *5*, 1873.